Thermal-hydraulic analysis of alternative cable-in-conduit conductors for the European DEMO hybrid Central Solenoid

Roberto Guarino[1,*], Monika Lewandowska[2], Aleksandra Dembkowska[2], Nikolay Bykovskiy[1], Xabier Sarasola[1], Kamil Sedlak[1]

[1] *École Polytechnique Fédérale de Lausanne (EPFL), Swiss Plasma Center (SPC), CH-5232 Villigen PSI, Switzerland*

[2] *West Pomeranian University of Technology, Szczecin, Al. Piastów 17, 70-310 Szczecin, Poland*

[*] *Corresponding author: roberto.guarino@epfl.ch*

Abstract

A hybrid design of the Central Solenoid is under study within the conceptual design phase of the European DEMO fusion reactor. It is based on HTS conductors in the innermost high-field layers, and Nb_3Sn and NbTi conductors for field values below 15 T. Since the resistance of the stainless steel jacket to mechanical fatigue drives the whole magnet design, alternative layouts of the cable-in-conduit conductors are aimed at decoupling the mechanical and hydraulic functions of the jacket itself. Thus, a reduced steel thickness, a smaller radial build of the coil and a larger magnetic flux are achievable. In this work, we analyse a new cable design based on filled conductors and tight He channels, both for the HTS and the LTS layers, and study their thermal-hydraulic performance by means of numerical simulations. After having introduced the geometrical and material details of the considered conductors, we present the model and assumptions introduced for estimating the AC losses, assumed as the only heating source. Finally, we discuss the resulting minimum temperature margin of the conductors and provide useful insights for future activities on conductor development.

Keywords

DEMO, superconducting magnets, central solenoid, numerical simulations, thermal-hydraulics

1. Introduction

Within the conceptual design activities of the European DEMOnstration fusion power plant (DEMO), a special attention is devoted to the design of the magnet system, which is based on superconducting coils [1-7]. The Central Solenoid (CS) is a fundamental component of the magnet system: thanks to its pulsed operation, it provides the required magnetic flux change

for initiating the plasma, as well as for generating and maintaining the plasma current during operation.

In order to reach the target magnetic flux (i.e., 250 Wb at the hexapolar null [8]), a large engineering current density is necessary. Therefore, a hybrid design of the CS has been conceived, exploiting a double-layered structure that optimises the use of the available space. Specifically, cable-in-conduit conductors based on high-temperature superconductors (HTS) are foreseen in the innermost high-field layers, whereas Nb_3Sn and NbTi-based conductors can be employed for magnetic field values in the range 6 to 15 T and below 6 T, respectively [9,10]. It has been proved that one of the main design drivers is the resistance to mechanical fatigue, which drives the design of the stainless steel jackets, and thus can limit the achievable value of the magnetic flux. The stainless steel jacket, in fact, has the double function of providing (i) an adequate mechanical strength to resist Lorentz forces and (ii) a hydraulic confinement for the helium flow. Alternative layouts of the cable-in-conduit conductors are aimed at decoupling the mechanical and hydraulic functions of the jacket, thus allowing a reduced steel thickness, and consequently a smaller radial build of the coil and a larger magnetic flux at the centre of the plasma [6]. Therefore, alongside the electromagnetic and mechanical design of the conductors, also their thermal-hydraulic performance must be investigated to evaluate their thermal stability.

In this work, we analyse a new cable design for the European DEMO CS, based on filled conductors and tight He channels, both for the HTS and the low-temperature superconducting (LTS) layers. We study their thermal-hydraulic performance in normal operating conditions by means of numerical simulations using the code THEA, CryoSoft [11], and considering the most critical points of the whole plasma scenario. In Section 2, we describe the design of the new HTS and LTS cable-in-conduit conductors, providing details of the main components and dimensions. In Section 3, we introduce the numerical model and the assumptions made. Finally, in Section 4 we discuss the main results and present ideas for future developments.

2. Conductor design

2.1 General layout

As displayed in Figure 1, the graded DEMO CS design mentioned above includes 10 double layers, of which L1 to L4 are made of HTS conductors, L5 to L16 are based on react-and-wind Nb_3Sn cables and L17 to L20 employ NbTi [6]. The cooling is realised through the forced flow of helium in tight (i.e., non-perforated) channels, thus the stainless steel jacket keeps only a structural function and presents a reduced thickness. The choice of two cooling channels

derives also from manufacturing purposes, since they realise an additional protection of the cable during the longitudinal (e.g., laser) welding of the jacket.

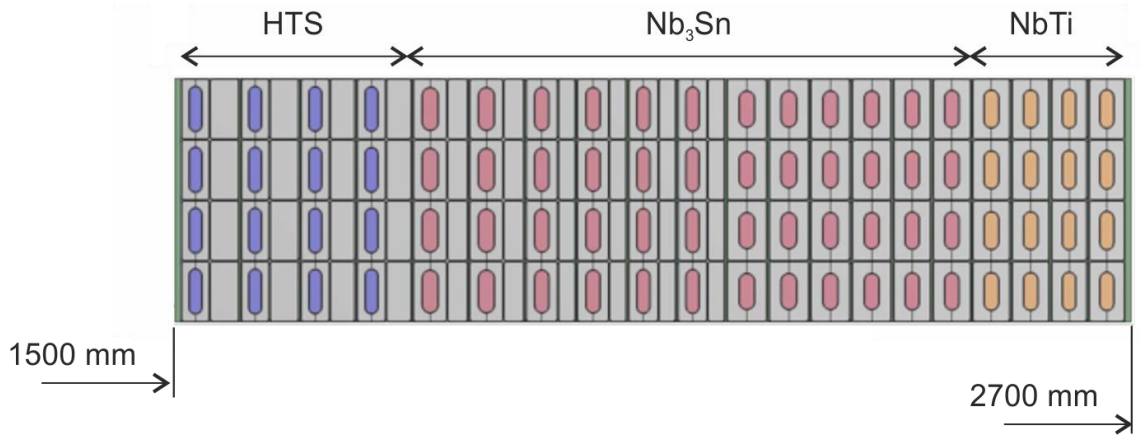

Figure 1 Hybrid design of the layer-wound DEMO CS modules, with indication of the internal and external radii and of the three conductor technologies employed.

In the case of the LTS (i.e., Nb_3Sn and NbTi) layers, the void space in the cable bundle is filled with solder. In the case of the HTS layers, instead, the filling is realised through an organic compound with high thermal conductivity. For all the layers, we consider a maximum operating current $I_{op,max}$ = 55.533 kA and a target copper current density J_{Cu} = 120.0 A mm^{-2} [6].
The segregated copper is arranged in two Rutherford cables of CuNi clad copper wires, which surround the superconducting strands and the helium channels. The selection of this geometry allows reduced AC losses during operation and derives from previous experiments [12]. We assume the following relation between the height of the Rutherford cable h_{Cu} and the copper strand diameter D_{Cu}:

$$h_{Cu} \approx \begin{cases} 1.9\, D_{Cu} & , \quad D_{Cu} < 2.7 \text{ mm} \\ 1.8\, D_{Cu} & , \quad D_{Cu} \geq 2.7 \text{ mm} \end{cases} \tag{1}$$

which derives from the experimental evidence [12] and takes into account the compaction of the cable. The actual void fraction, starting from a 10% target value, has been estimated through:

$$\varphi_{stabilizer} \approx 1 - \frac{N_{Cu}\pi \frac{D_{Cu}^2}{4}}{2h_{Cu}w_{Cu} - (4-\pi)R^2} \tag{2}$$

where N_{Cu} is the total number of copper strands.

2.2 HTS conductors

Figure 2 displays the proposed cable layout for the HTS conductors. The stacks of HTS tapes are arranged in 6 copper profiles with elongated shape and rounded edges, surrounded by two tight stainless steel helium channels on the two sides, which are in contact with the stainless steel jacket. The stacks are transposed in a Roebel cabling layout [6]. The void cable space is not available for helium flow, such as in non-solder filled conductors, but it is filled with an organic compound with high thermal conductivity: it should, in principle, guarantee the mechanical integrity of the cable in operation without a negative impact on the conductive cooling of the whole cross section, which takes place mostly through copper.

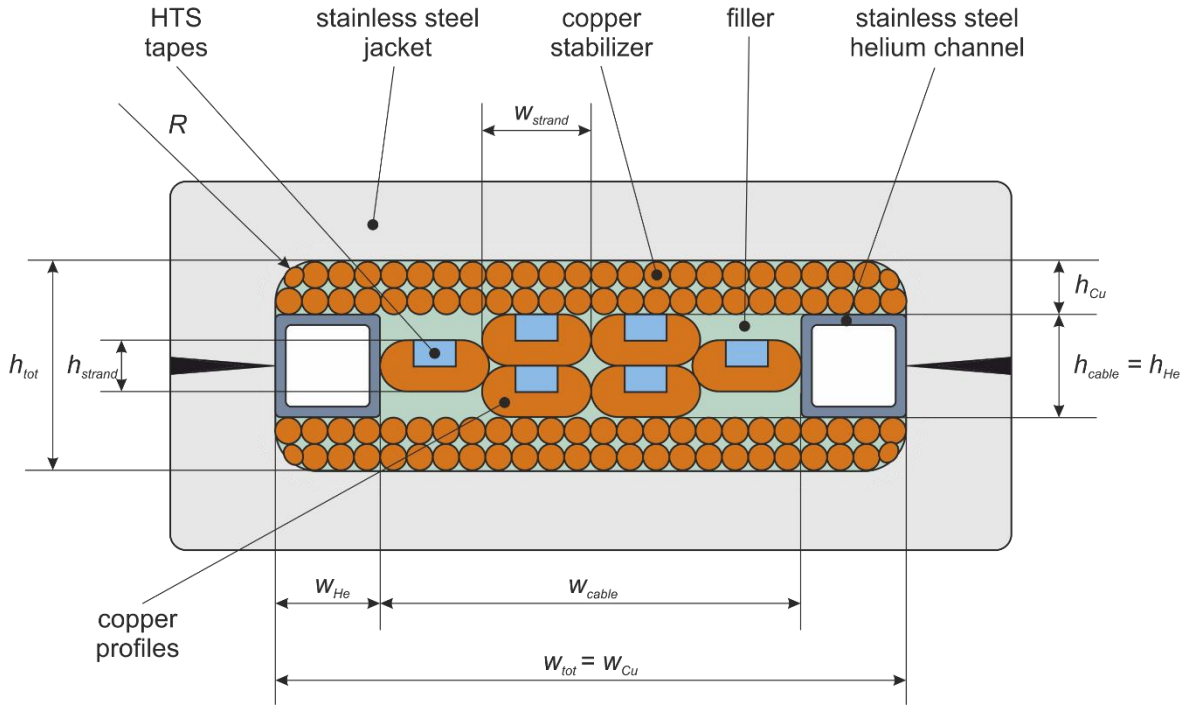

Figure 2 Schematic cross section of the proposed HTS conductors for the layers L1 to L4 of the DEMO CS, including main components and dimensions. The number of copper strands in the stabilizer may differ from reality.

The same Figure 2 reports the main dimensions and corresponding symbols used hereinafter. We keep fixed the overall (non-insulated) jacket width at the value w_{ext} = 74.36 mm. The total width of the cable space w_{tot} is also kept at the value provided in the preliminary design [6], whereas the total height of the cable space h_{tot} is adapted to the final cable and stabilizer dimensions. Consequently, the overall (non-insulated) jacket height h_{ext} has been computed

according to the minimum required stainless steel cross section obtained from structural analyses. For convenience, we make the following choices:

$$w_{tot} = w_{Cu} = w_{cable} + 2w_{He} \approx 3.95w_{strand} + 2w_{He} \quad (3a)$$

$$h_{tot} = h_{cable} + 2h_{Cu} = h_{He} + 2h_{Cu} \approx 2h_{strand} + 2h_{Cu} \quad (3b)$$

Table 1 reports the main characteristics and geometrical parameters of the proposed cable design for the HTS layers, i.e., from L1 to L4. For both the considered double-layers, the superconductor and copper cross sections are constant, thus the grading refers only to the stainless steel cross sections. High-performance second generation (2G) Rare-earth Barium Copper Oxide (ReBCO) superconducting tapes supplied from Shanghai Superconducting Technology Co. Ltd. (Shanghai, China) [13] are considered, with a 3.30 mm width and an approximate thickness of 80 μm. The material composition includes roughly 2 μm of superconductor, 2 μm of silver, 26 μm of copper and 50 μm of Hastelloy®. Note that the copper cross section in the HTS tapes has been neglected in the calculation of the total copper current density of the cable J_{Cu}. Details on the scaling law of the ReBCO tapes are reported in Appendix A.

Table 1 Main characteristics and geometrical parameters of the proposed HTS conductors for the layers L1 to L4 of the hybrid DEMO CS, divided by sub-coil (i.e., double layer).

	sub-coil (layers)	
	1	**2**
	(L1/L2)	**(L3/L4)**
superconducting cable		
subcable width, $w_{subcable}$ (mm)	8.00	8.00
subcable height, $h_{subcable}$ (mm)	4.00	4.00
number of subcables, $N_{subcable}$ (-)	6	6
number of superconducting tapes per subcable, N_{tapes} (-)	21	21
superconducting tapes cross section, A_{sc} (mm^2)	33.26	33.26
cable width, w_{cable} (mm)	31.60	31.60
cable height, h_{cable} (mm)	8.00	8.00
void fraction, φ_{sc} (%)	32.2	32.2

stabilizer		
total copper cross section, A_{Cu} (mm^2)	478.16	478.16
copper current density, J_{Cu} ($A\,mm^{-2}$)	116.1	116.1
segregated copper strand diameter, D_{Cu} (mm)	1.98	1.98
number of strand per Rutherford cable, $N_{Cu,strand}$ (-)	56	56
number of Rutherford cables, $N_{Cu,cable}$ (-)	2	2
Rutherford cable width, w_{Cu} (mm)	55.51	55.51
Rutherford cable height, h_{Cu} (mm)	3.76	3.76
copper void fraction, φ_{Cu} (%)	8.2	8.2
cooling		
helium channel width, w_{He} (mm)	11.96	11.96
helium channel height, h_{He} (mm)	8.00	8.00
helium channel thickness, t_{He} (mm)	1.00	1.00
conductor		
cable space total width, w_{tot} (mm)	55.51	55.51
cable space total height, h_{tot} (mm)	15.52	15.52
jacket inner radius, R (mm)	7.00	7.00
jacket outer radius, R_{ext} (mm)	3.00	3.00
non-insulated conductor total width, w_{ext} (mm)	74.36	74.36
non-insulated conductor total height, h_{ext} (mm)	34.16	34.90
stainless steel jacket cross section, A_{jacket} (mm^2)	1728.00	1783.50
stainless steel strip cross section, A_{strip} (mm^2)	2594.80	2223.00
filler cross section, A_{filler} (mm^2)	112.14	112.14

2.3 LTS conductors

Figure 3 displays the proposed cable layout for the LTS conductors. We propose a flat superconducting cable at the centre, and, again, two tight stainless steel helium channels on the two sides, which are in contact with the stainless steel jacket. Additionally, a thin stainless steel strip is inserted between the superconducting subcables, for reducing the AC losses.

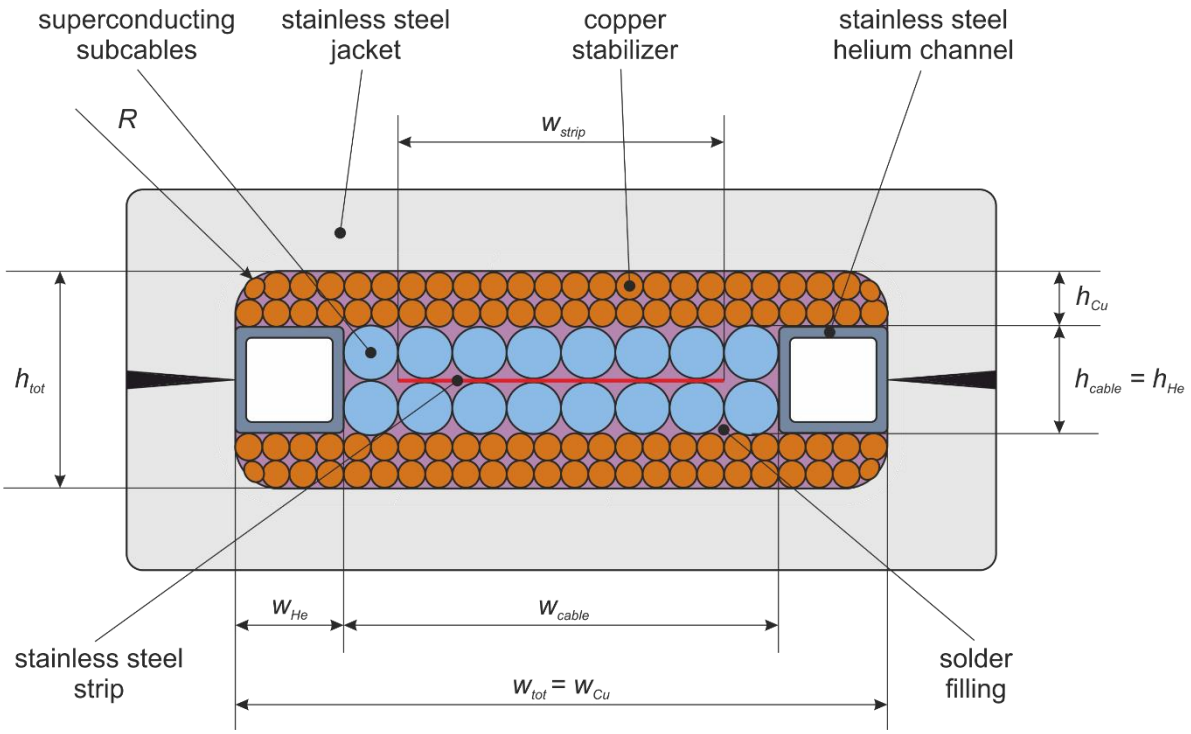

Figure 3 Schematic cross section of the proposed LTS conductors for the layers L5 to L20 of the DEMO CS, including main components and dimensions. The number of copper strands in the stabilizer and of superconducting subcables may differ from reality.

The same Figure 3 reports the main dimensions and corresponding symbols used hereinafter. Again, we keep fixed the overall (non-insulated) jacket width at the value w_{ext} = 74.36 mm and adjust the other dimensions according to the final cable and stabilizer geometries, as well as to the required stainless steel cross section.

For convenience, in analogy with Equations (3), we make use of the following geometrical relations:

$$w_{tot} = w_{Cu} = w_{cable} + 2w_{He} \tag{4a}$$

$$h_{tot} = h_{cable} + 2h_{Cu} = h_{He} + 2h_{Cu} \tag{4b}$$

The relation between cable width and height is given by the following expression:

$$w_{cable}h_{cable} = \frac{A_{sc} + A_{Cu,strand}}{\cos\theta\,(1 - \varphi_{sc})} + w_{strip}h_{strip} \tag{5}$$

where h_{strip} is the thickness of the stainless steel strip, and the value of w_{strip} has been taken in the order of 90% of w_{cable}.

Two possible layouts of the superconducting subcables are considered, here denoted as "A" and "B", as shown in Figure 4. The first cabling stage can present 19 or 7 superconducting strands, arranged in a 1+6+12 or a 1+6 layout, respectively. The subcable diameter $D_{subcable}$ is computed, respectively, according to:

$$D_{subcable,A} = \frac{h_{cable}}{2} \approx 4.5\, D_{sc} \tag{6a}$$

$$D_{subcable,B} = \frac{h_{cable}}{2} \approx 2.85\, D_{sc} \tag{6b}$$

where D_{sc} is the diameter of the superconducting strand.

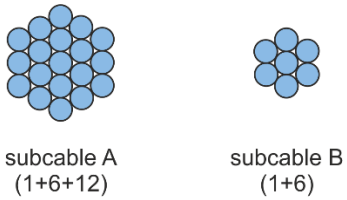

Figure 4 Possible layouts of the first cabling stage of the LTS conductors for the DEMO CS.

We consider a copper-to-non-copper ratio of 1.0 for Nb_3Sn and 1.5 for NbTi strands. In addition, for the Nb_3Sn and NbTi layers we use a target void fraction of 20 and 30%, respectively. The actual void fraction has been obtained through an iterative procedure starting from Equation (5), i.e.:

$$\varphi_{sc} = 1 - \frac{N_{sc}\pi \frac{D_{sc}^2}{4}}{\cos\theta \left(h_{cable} w_{cable} - h_{strip} w_{strip}\right)} \tag{7}$$

Tables 2 and 3 report the main characteristics and geometrical parameters of the proposed cable design for the Nb_3Sn layers, i.e., from L5 to L16, and for the NbTi layers, i.e., from L17 to L20. Details on the scaling laws employed for Nb_3Sn and NbTi strands are reported in Appendices B and C, respectively.

Table 2 Main characteristics and geometrical parameters of the proposed Nb_3Sn conductors for the layers L5 to L16 of the hybrid DEMO CS, divided by sub-coil (i.e., double layer).

	sub-coil					
	3	**4**	**5**	**6**	**7**	**8**
	(L5/L6)	**(L7/L8)**	**(L9/L10)**	**(L11/L12)**	**(L13/L14)**	**(L15/L16)**
superconducting cable						
cabling pattern	1+6+12	1+6+12	1+6+12	1+6+12	1+6	1+6
strand diameter, D_{strand} (mm)	1.35	1.05	0.85	0.75	1.00	0.90
number of strand per subcable, N_{strand} (-)	19	19	19	19	7	7
number of subcables, $N_{subcable}$ (-)	13	13	13	12	13	12
pure superconductor cross section, A_{sc} (mm^2)	176.78	106.94	70.08	50.36	35.74	26.72
cable width, w_{cable} (mm)	39.49	30.71	24.86	20.25	18.53	15.39
cable height, h_{cable} (mm)	11.72	9.14	7.43	6.61	5.13	4.60
stainless steel strip width, w_{strip} (mm)	35.00	25.00	20.00	20.00	15.00	10.00
stainless steel strip thickness, h_{strip} (mm)	0.20	0.20	0.20	0.20	0.20	0.20
void fraction, φ_{sc} (%)	19.7	19.6	19.6	19.4	19.4	19.4
stabilizer						
total copper cross section, A_{Cu} (mm^2)	475.25	471.87	469.12	486.77	477.71	465.09
copper current density, J_{Cu} ($A\,mm^{-2}$)	116.9	117.7	118.4	114.1	116.3	119.4
segregated copper cross section, $A_{Cu,extra}$ (mm^2)	298.47	364.93	399.04	436.41	441.97	438.37
segregated copper strand diameter, D_{Cu} (mm)	1.81	2.20	2.35	3.15	3.17	3.05
number of strand per Rutherford cable, $N_{Cu,strand}$ (-)	58	48	46	28	28	30
Rutherford cable width, w_{Cu} (mm)	52.70	52.77	53.93	44.22	44.40	45.55
Rutherford cable height, h_{Cu} (mm)	3.44	4.18	4.47	5.67	5.71	5.49
copper void fraction, φ_{Cu} (%)	8.5	9.9	11.5	7.3	8.9	8.4
cooling						
helium channel width, w_{He} (mm)	5.26	11.03	14.53	11.99	12.94	14.80

helium channel height, h_{He} (mm)	10.85	9.14	7.43	6.61	5.13	4.10
helium channel thickness, t_{He} (mm)	1.00	1.00	1.00	1.00	1.00	1.00
conductor						
cable space total width, w_{tot} (mm)	52.70	52.77	53.93	44.22	44.40	45.55
cable space total height, h_{tot} (mm)	18.59	17.50	16.36	17.95	16.55	15.58
jacket inner radius, R (mm)	6.50	6.50	6.00	6.00	5.00	5.00
jacket outer radius, R_{ext} (mm)	3.00	3.00	3.00	3.00	3.00	3.00
non-insulated conductor total width, w_{ext} (mm)	74.36	74.36	74.36	74.36	74.36	74.36
non-insulated conductor total height, h_{ext} (mm)	40.09	39.00	36.54	48.66	47.44	44.94
stainless steel jacket cross section, A_{jacket} (mm^2)	2090.70	2020.40	1873.40	2863.70	2822.50	2683.80
stainless steel strip cross section, A_{strip} (mm^2)	1776.90	1479.50	1479.50	-	-	-
solder-filled cross section, A_{filler} (mm^2)	116.49	91.14	81.86	57.62	57.82	50.69

Table 3 Main characteristics and geometrical parameters of the proposed NbTi conductors for the layers L17 to L20 of the hybrid DEMO CS, divided by sub-coil (i.e., double layer).

	sub-coil	
	9 (L17/L18)	**10 (L19/L20)**
superconducting cable		
cabling pattern	1+6+12	1+6
strand diameter, D_{strand} (mm)	0.80	0.85
number of strand per subcable, N_{strand} (-)	19	7
number of subcables, $N_{subcable}$ (-)	13	14
pure superconductor cross section, A_{sc} (mm^2)	49.66	22.24
cable width, w_{cable} (mm)	23.40	16.96
cable height, h_{cable} (mm)	7.99	5.01
stainless steel strip width, w_{strip} (mm)	20.00	15.00
stainless steel strip thickness, h_{strip} (mm)	0.20	0.20
void fraction, φ_{sc} (%)	29.4	28.9

stabilizer		
total copper cross section, A_{Cu} (mm^2)	472.53	470.80
copper current density, J_{Cu} ($A\,mm^{-2}$)	117.5	118.0
segregated copper cross section, $A_{Cu,extra}$ (mm^2)	398.04	437.44
segregated copper strand diameter, D_{Cu} (mm)	2.73	2.95
number of strand per Rutherford cable, $N_{Cu,strand}$ (-)	34	32
Rutherford cable width, w_{Cu} (mm)	46.42	47.22
Rutherford cable height, h_{Cu} (mm)	4.91	5.31
copper void fraction, φ_{Cu} (%)	9.3	9.6
cooling		
helium channel width, w_{He} (mm)	11.51	15.13
helium channel height, h_{He} (mm)	7.99	5.01
helium channel thickness, t_{He} (mm)	1.00	1.00
conductor		
cable space total width, w_{tot} (mm)	46.42	47.22
cable space total height, h_{tot} (mm)	17.81	15.63
jacket inner radius, R (mm)	4.50	4.50
jacket outer radius, R_{ext} (mm)	3.00	3.00
non-insulated conductor total width, w_{ext} (mm)	74.36	74.36
non-insulated conductor total height, h_{ext} (mm)	46.03	43.25
stainless steel jacket cross section, A_{jacket} (mm^2)	2621.00	2503.60
stainless steel strip cross section, A_{strip} (mm^2)	-	-
solder-filled cross section, A_{filler} (mm^2)	91.86	66.73

3. Thermal-hydraulic model

3.1 Plasma scenario and magnetic field

The plasma scenario considered for the operation of the DEMO CS is displayed in Figure 5, where it is represented in terms of operating current $I_{op}(t)$. The main points of the scenario are the PRE-MAGnetisation phase (PREMAG), the Start Of Flat-top (SOF), the End Of Flat-top (EOF) and the End of Plasma (EOP). At PREMAG and EOF the current reaches its maximum value $I_{op,max}$, but with the opposite sign. We also assume the presence of a plasma BreakDown (BD), which lasts for 0.8 s after PREMAG and is characterized by a linear current decay down to 94.33% of $I_{op,max}$ [14].

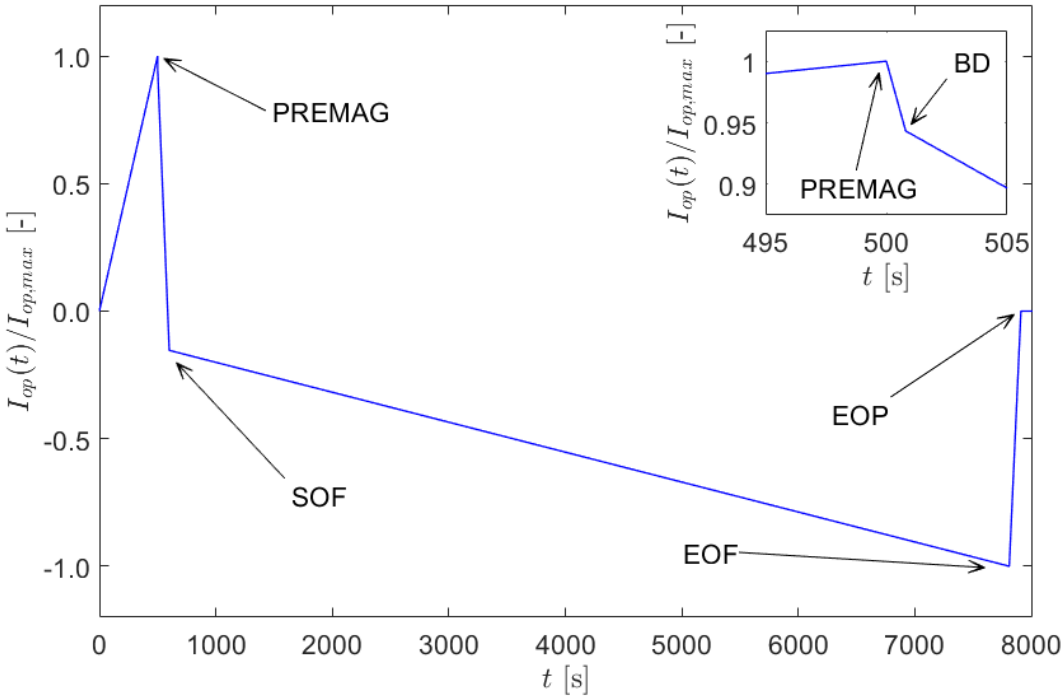

Figure 5 Plasma scenario considered in the thermal-hydraulic analysis of the DEMO CS conductors, displayed as current ratio as function of time. Inset: zoom around the PREMAG and plasma BD.

A 2D finite-element model has been used to compute the distribution of the magnetic field along the conductor length of each layer in the DEMO CS1 module during the PREMAG, SOF and EOF points of the plasma scenario [6]. Since the magnetic field distribution is not available for every value of $I_{op}(t)$, we have employed a linear interpolation of both field components (i.e., radial and axial) between each pair of known points of the plasma scenario. We believe this is a good approximation of the real time dependence of the magnetic field, whose absolute values is not necessarily linearly proportional to the magnitude of the operating current. The maximum values of the magnetic field are reported at PREMAG, and are displayed in Figure 6 for the odd CS layers.

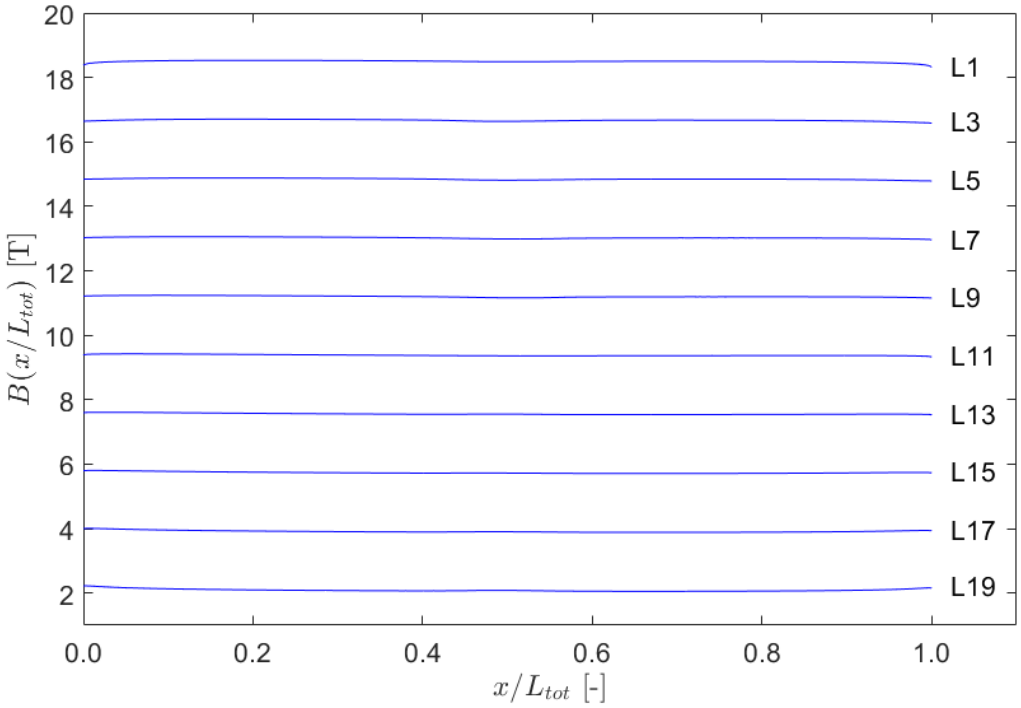

Figure 6 Distribution of the magnitude of magnetic field along the (dimensionless) conductor coordinate in the odd layers of the DEMO CS1, computed at the PREMAG through 2D finite-element simulations.

3.2 Heat loads

We assume that the CS conductors are subjected only to AC losses, which are dependent both in time and in space (i.e., along the conductor length), due to the time and space variation of the magnetic field, respectively. They are applied as a distributed heat load. Here we neglect all the static heat load components, e.g., those due to radiation and to the conduction from the gravity supports of the Toroidal Field (TF) coils.

The considered AC losses include the coupling and hysteresis losses, both depending on the conductor geometry and size. For the LTS layers, which are based on multi-filamentary superconducting strands, the coupling power losses per unit conductor length (in W m^{-1}) are computed according to [15,16]:

$$\dot{Q}_c = \frac{n\tau}{\mu_0} A_{sc+\mathrm{Cu}} \dot{B}^2 \tag{8a}$$

where $A_{sc+\mathrm{Cu}}$ is the total cross section of the strands, $\dot{B}$ the time derivative of the time-varying magnetic field $B(t)$, $\mu_0 = 4\pi \cdot 10^{-7}$ H m^{-1} the magnetic permeability of vacuum, τ the coupling

loss time constant and n a dimensionless shape parameter. Since τ is, in principle, unknown for the proposed cable design, here we perform a parametric analysis by using the following values of $n\tau$: 0.075, 0.150, 0.250 and 0.400 s. The choice of this range derives from the reference value used for non-solder-filled conductors of the DEMO CS (i.e., 0.075 s [15,17]) and from experimental tests of a previous version of solder-filled react-and-wind conductor [18].
In the case of the HTS layers, instead, considering the geometry shown in Figure 2, we use the formula available for Rutherford cables [16]:

$$\dot{Q}_c = \frac{1}{120}\frac{N(N-1)LH^2}{R_\perp}\dot{B}^2 \tag{8b}$$

which has the same dependence with $\dot{B}$ but further includes information on the geometry of the N slabs (i.e., the stacks of HTS tapes) in terms of twist pitch L and conductor width H. $R_\perp$ is a transverse electrical resistance, here assumed approximately equal to $1 \cdot 10^{-5}\, N/L$.
The hysteresis power losses per unit conductor length (in W m^{-1}) are computed according to [15,16]:

$$\dot{Q}_h = \Psi d J_c A_{sc} \dot{B} \tag{9}$$

where J_c is the critical current density and A_{sc} the pure superconductor cross section. The dimensionless factor Ψ depends on the considered geometry and it is equal to 1/4 for a slab and $2/(3\pi)$ for a cylinder, whereas d is a characteristic dimension and is assumed equal to the width of the HTS stack or to the diameter of the superconducting filaments, depending on the considered CS layer. Here we assume d = 2.00 mm for the HTS stacks and d = 10 μm for the LTS filaments.
Finally, the total heat load per unit length of conductor is given by:

$$\dot{Q}_{tot}(x,t) = \dot{Q}_c(x,t) + \dot{Q}_h(x,t) \tag{10}$$

where the dependence on t and on the coordinate x is included in $\dot{B}$ in Equations (8,9).
The main assumption used in modelling the AC losses is that we employ formulae valid only for fully penetrated conductors. In addition, Equation (9) assumes an infinite slab or cylinder

length, but the introduced error is negligible at high fields; whereas J_c is considered constant and taken at the maximum field conditions.

3.3 Numerical simulations

The thermal-hydraulics numerical simulations have been performed using the code THEA, CryoSoft [11]. Each CS layer has been modelled as a one-dimensional conductor including seven parallel thermal components (i.e., stainless steel jacket, stainless steel cooling channels, copper stabilizer, superconducting stacks, copper profiles, and filler) for layers 1 to 4, and five parallel thermal components (i.e., stainless steel jacket, stainless steel cooling channels, copper stabilizer, superconducting cable, and stainless steel strip, if present) for layers 5 to 20. In every case, one hydraulic component, corresponding to the helium flow in both cooling channels, has been employed.

We apply an inlet pressure of 6.0 bar and impose a pressure drop of 1.0 bar (i.e., an outlet pressure of 5.0 bar) along the whole conductor length. The resulting helium mass flow rate in the hydraulic component is an output of the simulations. A 4.5 K temperature is applied as initial condition along the whole conductor length, both for the helium and for the solid components. The simulations can be considered adiabatic, because a zero heat load has been assigned to the inlet and the outlet.

The helium pressure drop in the cooling channels has been estimated through the friction factor correlation for smooth rectangular ducts, which, in transition and turbulent regimes, reads [19]:

$$f = \begin{cases} \left(1.0875 - 0.1125\dfrac{h_{He}}{w_{He}}\right)\left(5.4 \cdot 10^{-3} + 2.3 \cdot 10^{-8}\mathrm{Re}^{1.5}\right), 2300 < \mathrm{Re} \leq 4000 \\ \left(1.0875 - 0.1125\dfrac{h_{He}}{w_{He}}\right)\left(1.28 \cdot 10^{-3} + 0.1143\mathrm{Re}^{-0.311}\right), 4000 < \mathrm{Re} < 1 \cdot 10^{7} \end{cases} \quad (11)$$

where the channel dimensions h_{He} and w_{He} are given in Figures 2 and 3, and Re is the Reynolds number.

The convective heat transfer coefficient (i.e., between the helium flow and the internal walls of the cooling channels) in turbulent regime has been estimated through the Dittus-Boelter correlation for smooth ducts [20]:

$$\mathrm{Nu} = 0.023\mathrm{Re}^{0.8}\mathrm{Pr}^{0.4} \quad (12)$$

where Nu and Pr are the Nusselt and Prandtl numbers, respectively.

The heat conduction between solid components, instead, has been modelled by using a thermal contact resistance given by [15,17]:

$$R_s = \frac{1}{h_s P_{contact}} \quad (13)$$

where $P_{contact}$ is the contact perimeter of each pair of thermal components and h_s = 500 W m^{-2} K^{-1} has been assumed conservatively as the equivalent heat transfer coefficient. Furthermore, the simulation setup includes the inter-turn heat transfer, i.e., within each CS layer the conductor jacket is thermally coupled with each adjacent turn of the jacket itself. A 4.00 mm insulation thickness has been considered for this purpose.

The system has been discretised with a grid of 2-node linear elements, with a constant element length of 1.0 m, and the Crank-Nicolson method has been employed for the time integration. An adaptive time stepping has been used, with a maximum time step of 0.05 s.

4. Results and discussion

4.1 Helium mass flow rates

Figure 7 reports the helium mass flow rate $\dot{m}$ in each conductor, from the THEA simulations. We display only the odd layers since, as anticipated above, the winding is realised in double-layers and thus each even layer has exactly the same cross section of the previous one, so it features only marginally smaller mass flow rate due to a slightly larger hydraulic length. The total mass flow rate needed for the proposed design of the DEMO CS1 is approximately 216.0 g s^{-1}.

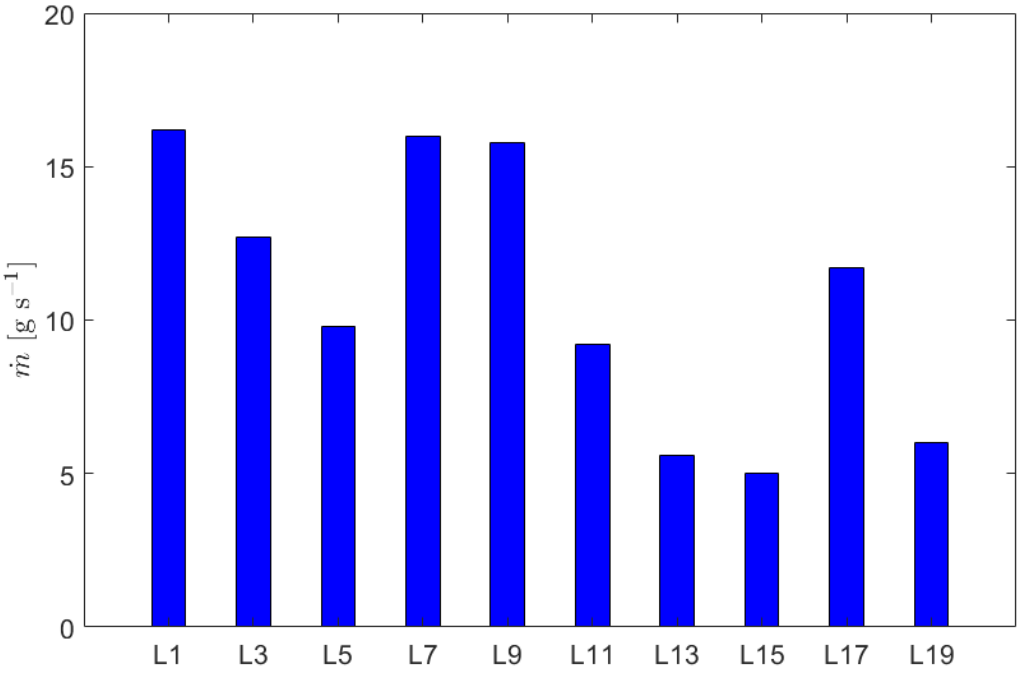

Figure 7 Total supercritical helium mass flow rate in the odd layers of the DEMO CS1, obtained from numerical simulations in THEA.

We observe that in most of the conductors the supercritical helium mass flow rate is close to or larger than 10.0 g s^{-1}, except for L13, L15 and L19, which have $\dot{m} \approx 5.0$ g s^{-1}. However, these layers are not critical in terms of magnetic field and current sharing temperature, thus they are expected to guarantee a safe operation despite the reduced heat removal capability. This is beneficial for optimising the overall operation and efficiency of the DEMO cryo-plant [21]. On the contrary, the most critical layers for each conductor technology (i.e., L1 for HTS, L5 for Nb_3Sn and L17 for NbTi) present larger values of $\dot{m}$ if compared to the subsequent (i.e., less critical) layers.

Furthermore, the use of tight cooling channels allows to realise a low-friction flow and thus to achieve large mass flow rates, if compared, for instance, to the helium flow in the cable bundle [22].

4.2 Temperature margin evaluation

The temperature margin has been evaluated along the conductor coordinate x (with $x = 0$ corresponding to the inlet and $x = L_{tot}$ to the outlet), as:

$$\Delta T(x,t) = T_{cs}(x,t) - T_{op}(x,t) \tag{14}$$

where T_{cs} is the current sharing temperature, obtained from the scaling law of the superconductor at the local value of field and current, and T_{op} is the operating temperature of the conductor resulting from the numerical simulations. The quantity of interest in our thermal-hydraulic assessment is the minimum temperature margin along the conductor length, i.e.:

$$\Delta T_{min}(x,t) = \min\{\Delta T(x,t)\} = \min\{T_{cs}(x,t) - T_{op}(x,t)\} \tag{15}$$

The first results that has been assessed is the location (in time) of the minimum temperature margin along the conductor length. The most critical part of the plasma scenario is the BD, in which the fast current decay produces ramps in the magnetic field up to about 1 T s^{-1}, thus generating very large heat loads, according to Equations (8-10). However, during BD the absolute value of B decreases and thus the T_{cs} increases, and therefore, despite the likely increase in T_{op}, the minimum temperature margin may not be measured for t = 500.8 s. This is clarified in Figure 8, which shows the trend of ΔT_{min} as function of time from the PREMAG to plasma BD, i.e., from t = 500.0 to 500.8 s, for the most critical layers for each conductor technology (i.e., HTS, Nb_3Sn and NbTi). While in the case of LTS conductors the minimum temperature margin is detected at the PREMAG, because of the smallest value of T_{cs}, the HTS layer presents a minimum value around 0.1 s after the start of the plasma BD phase.

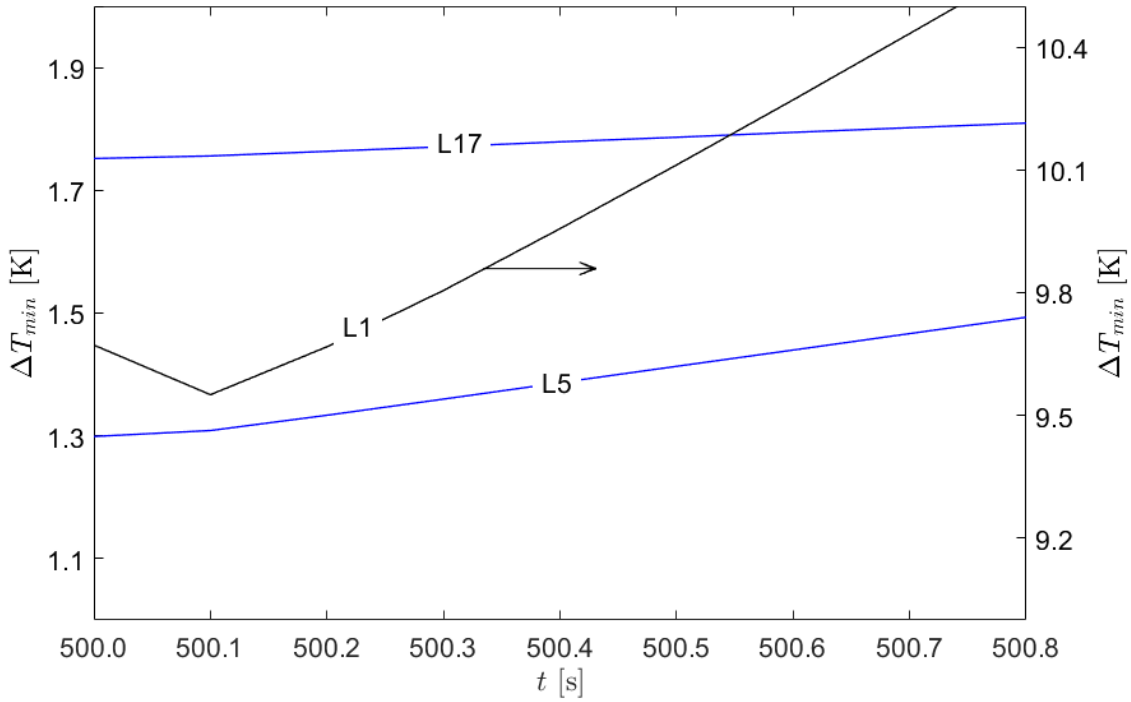

Figure 8 Minimum value of the temperature margin along the conductor length, from Equation (15), as function of time between the PREMAG and plasma BD in the most critical of the DEMO CS1 for each conductor technology (i.e., HTS, Nb_3Sn and NbTi), obtained from numerical simulations in THEA.

The THEA results have been validated by comparison of the helium mass flow rate, as well as of the temperature, pressure and temperature margin profiles along the conductors, with the respective results computed with the steady-state model presented in Refs. [23,24]. As an example, we report in Figure 9 the value of $\Delta T(x)$, computed according to Equation (14), for L5 at the EOF. We observe that the two models are in a perfect agreement, with a maximum difference in the order of 0.20% at the location of the minimum temperature margin, i.e., around the centre of the conductor length.

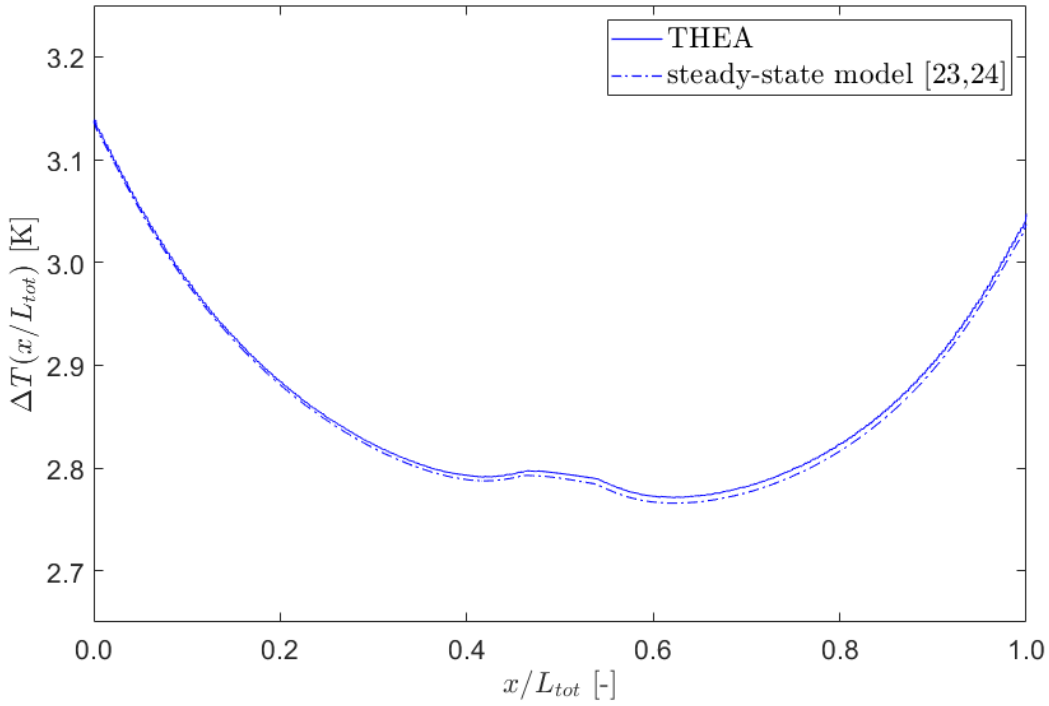

Figure 9 Comparison between the numerical simulations performed in THEA and obtained through the steady-state model (see Refs. [23,24]) in terms of temperature margin as function of the (dimensionless) conductor coordinate at the EOF for the L5 conductor of the DEMO CS1.

4.3 HTS conductors

Figure 10 displays the temperature margin along the conductor length for the two HTS (odd) layers. Since L3 present exactly the same cable design of L1, as already outlined in Table 1, but it is subjected to a lower magnetic field, it is slightly overdesigned. From $x/L_{tot} \approx 0.5$ onwards, the ΔT profile becomes almost flat, due to the analogous trend of $T_{op}(x)$.

In the same Figure 10, we plot also the ratio between the operating current density J_{op} and the critical current density value provided by the scaling law (see Appendix A). We observe that a safe design is guaranteed, thanks to a ratio of about 65.5% in the worst conditions (i.e., for L1 at $x/L_{tot} \approx 0.9$). This is below the target design value of 80% of J_c [6], thus in a future design iteration the conductor characteristics, i.e., *in primis* the number of HTS tapes in each stack, can be further optimised. It must be pointed out, however, that the operating conditions of the HTS conductors could be more critical in the DEMO CS3 module, which presents a larger perpendicular component of the magnetic field and thus, consequently, a smaller J_c (see Appendix A). This investigation is the objective of a future study.

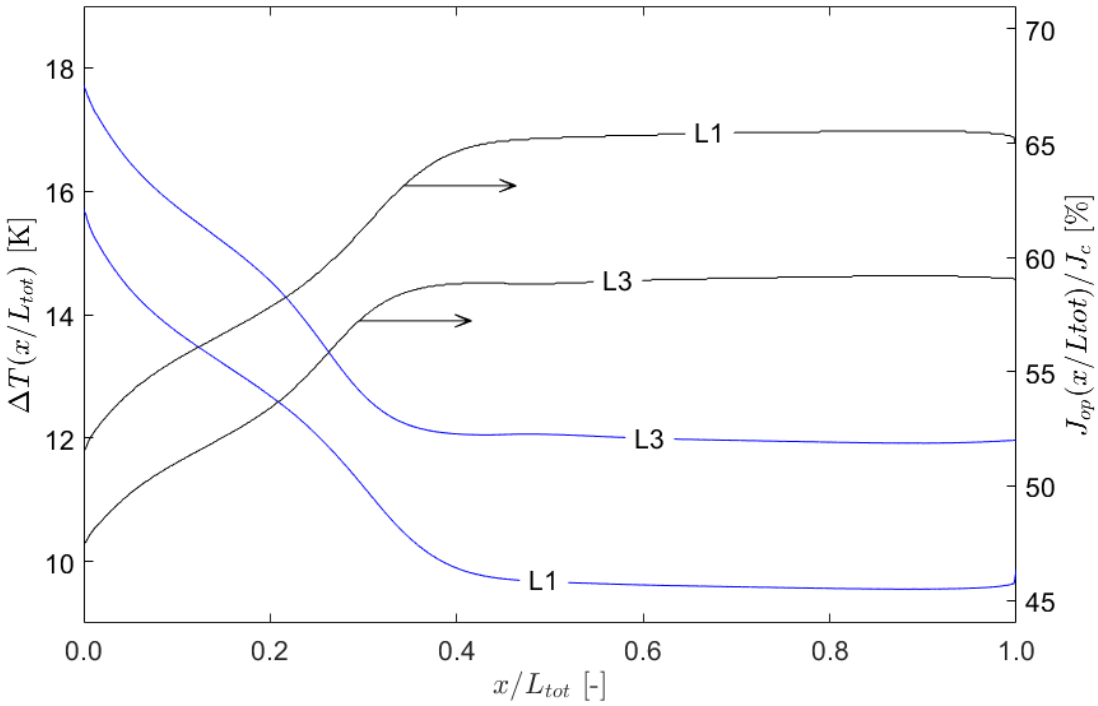

Figure 10 Temperature margin along the (dimensionless) conductor coordinate, from Equation (14) (left axis), and operating current-to-critical current ratio (right axis) at t = 500.1 s for the HTS conductors of the DEMO CS1.

4.4 LTS conductors

Figure 11 displays the global minimum temperature margin computed in all the LTS double-layers, as function of $n\tau$. As explained above, only the odd layer is reported here.

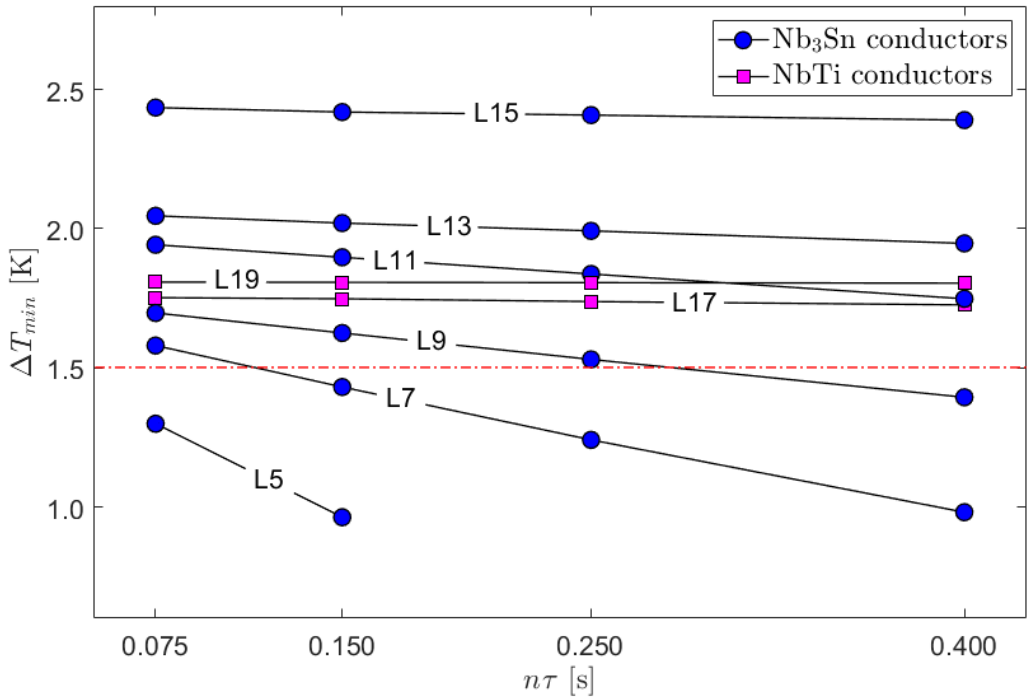

Figure 11 Minimum value of the temperature margin along the conductor length, from Equation (15), in the odd layers of the DEMO CS1, obtained from numerical simulations in THEA. The dashed line represents the target design value.

As expected, a larger value of $n\tau$ increases the heat deposited onto the conductor, according to Equation (8a), and consequently the operating temperature becomes larger and the minimum temperature margin smaller. The decrease in ΔT_{min} is approximately linear with $n\tau$. We observe that the target temperature margin (i.e., the design value used in the preliminary sizing of the superconductor [6]) of 1.50 K is met only for the smallest values of $n\tau$, in the case of the layers subjected to magnetic fields larger than 11 T. An exception is represented by L5, which is the most critical Nb_3Sn-based conductor in terms of magnetic field, and which does not reach the target ΔT_{min} even for the baseline value $n\tau$ = 0.075 s. This might be due to a too small helium cross section, also evident from the mass flow rate data in Figure 7, thus in a future design iteration a more efficient cooling (e.g., with larger cooling channels) must be implemented.
The layers in low-field region, instead, present a safe temperature margin for any value of $n\tau$, thus they are stable against AC losses also in the case of solder filling. This is especially true for the NbTi conductors, whose very low coupling losses make ΔT_{min} almost independent on $n\tau$, with a maximum variation below 0.03 K between $n\tau$ = 0.075 s and 0.400 s.

5. Conclusions

We have presented the thermal-hydraulic numerical simulations of a filled conductor design for the hybrid DEMO CS1 module. The proposed cable design of the HTS and LTS cable-in-conduit conductors is based on filling the available void space with high-conductivity organic compounds and with solder, respectively. Whereas the cooling by supercritical helium is realised through the forced flow in two tight stainless steel channels. This solution, therefore, decouples the hydraulic and structural functions of the jacket, thus allowing an increased resistance to mechanical fatigue.

The cable stability is affected solely by the heat load generated by the AC losses, which produces a minimum temperature margin at the end of the PREMAG and/or during the plasma BD. The results show that the HTS layers present a safe design margin, if considering both the temperature margin and the ratio between operating and critical current density. Thus, they are most likely suitable also for the CS3 module, which presents more unfavourable orientations of the magnetic field. The LTS layers, instead, have been investigated for different coupling loss time constants, i.e., in the typical range for solder-filled react-and-wind conductors. The layers operating in high fields (i.e., larger than 11 T) do not seem to sustain large heat loads, and thus they are unstable if solder-filled. Instead, from L11 to L20 the AC losses have a minor effect on the minimum temperature margin, which is well above the design target of 1.50 K.

In a future design iteration of the DEMO CS conductors, the choice of solder filling will be made based on experimental testing and an updated version of the most critical LTS layers, e.g., with an increased heat removal capability, will be studied. Future quench propagation studies, in addition, should potentially include also the inter-layer thermal coupling, which may affect the thermal performance of adjacent layers in case of concentrated hot spots [25].

Acknowledgments

The authors acknowledge Dr. Davide Uglietti for fruitful discussions, and the technical support of the Paul Scherrer Institut (PSI).

This work has been carried out within the framework of the EUROfusion Consortium, funded by the European Union via the Euratom Research and Training Programme (Grant Agreement No 101052200 – EUROfusion). Views and opinions expressed are however those of the authors only and do not necessarily reflect those of the European Union or the European Commission. Neither the European Union nor the European Commission can be held responsible for them.

This scientific paper has been published as part of the international project called 'PMW', co-financed by the programme of the Polish Ministry of Science and Higher Education within the

framework of the scientific financial resources for 2022 under the contract No. 5251/HEU-EURATOM/2022/2.

References

[1] K. Sedlak, V.A. Anvar, N. Bagrets, M.E. Biancolini, R. Bonifetto, F. Bonne, D. Boso, A. Brighenti, P. Bruzzone, G. Celentano, A. Chiappa, V. D'Auria, M. Dan, P. Decool, A. della Corte, A. Dembkowska, O. Dicuonzo, I. Duran, M. Eisterer, A. Ferro, C. Fiamozzi Zignani, W.H. Fietz, C. Frittitta, E. Gaio, L. Giannini, F. Giorgetti, F. Gömöry, X. Granados, R. Guarino, R. Heller, C. Hoa, I. Ivashov, G. Jiolat, M. Jirsa, B. Jose, R. Kembleton, M. Kumar, B. Lacroix, Q. Le Coz, M. Lewandowska, A. Maistrello, N. Misiara, L. Morici, L. Muzzi, S. Nicollet, A. Nijhuis, F. Nunio, C. Portafaix, G. Romanelli, X. Sarasola, L. Savoldi, B. Stepanov, I. Tiseanu, G. Tomassetti, A. Torre, S. Turtù, D. Uglietti, R. Vallcorba, L. Viererbl, M. Vojenciak, C. Vorpahl, K.P. Weiss, R. Wesche, M.J. Wolf, L. Zani, R. Zanino, A. Zappatore, V. Corato, Advance in the conceptual design of the European DEMO magnet system, *Superconductor Science and Technology* **33** (2020) 044013.

[2] R. Wesche, X. Sarasola, R. Guarino, K. Sedlak, P. Bruzzone, Parametric study of the TF coil design for the European DEMO, *Fusion Engineering and Design* **164** (2021) 112217.

[3] M. Kumar, R. Guarino, K. Sedlak, X. Sarasola, P. Bruzzone, Alternative PF coil winding pack design for the EU DEMO, *IEEE Transactions on Applied Superconductivity* **31** (2021) 4201305.

[4] R. Guarino, R. Wesche, X. Sarasola, K. Sedlak, P. Bruzzone, A design proposal for the European DEMO superconducting bus bars and current leads, *Fusion Engineering and Design* **169** (2021) 112430.

[5] V. Corato, C. Vorpahl, K. Sedlak, V.A. Anvar, J. Bennet, M.E. Biancolini, F. Bonne, R. Bonifetto, D.P. Boso, A. Brighenti, P. Bruzzone, G. Celentano, A. della Corte, G. De Marzi, V. D'Auria, F. Demattè, A. Dembkowska, O. Dicuonzo, C. Fiamozzi Zignani, W.H. Fietz, C. Frittitta, L. Giannini, F. Giorgetti, R. Guarino, R. Heller, C. Hoa, M. Huguet, G. Jiolat, M. Kumar, B. Lacroix, M. Lewandowska, N. Misiara, L. Morici, L. Muzzi, D.S. Nickel, S. Nicollet, A. Nijhuis, F. Nunio, C. Portafaix, X. Sarasola, L. Savoldi, I. Tiseanu, G. Tomassetti, A. Torre, S. Turtù, D. Uglietti, R. Vallcorba, K.P. Weiss, R. Wesche, M.J. Wolf, K. Yagotintsev, L. Zani, R. Zanino, A.

Zappatore, The DEMO magnet system – Status and future challenges, *Fusion Engineering and Design* **174** (2022) 112971.

[6] V. Corato, P. Bruzzone, N. Bykovskiy, G. Celentano, A. della Corte, F. Demattè, S. Fink, W.H. Fietz, L. Muzzi, X. Sarasola, K. Sedlak, A. Torre, L. Zani, G. Federici, Strategy for developing the EU-DEMO magnet system in the concept design phase, *IEEE Transactions on Applied Superconductivity* **32** (2022) 4201407.

[7] F. Demattè, P. Bruzzone, X. Sarasola, K. Sedlak, V. Corato, Preliminary design of a high current R&W TF coil conductor for the EU DEMO, *IEEE Transactions on Applied Superconductivity* **32** (2022) 4202504.

[8] R. Ambrosino, Equilibria EOF/SOF 2018 PhysMag, 9th July 2019, https://idm.euro-fusion.org/?uid=2NV5BB.

[9] R. Wesche, X. Sarasola, K. Sedlak, N. Bykovskiy, B. Stepanov, D. Uglietti, P. Bruzzone, DEMO central solenoid design based on the use of HTS sections at highest magnetic field, *IEEE Transactions on Applied Superconductivity* **28** (2018) 4203605.

[10] R. Wesche, X. Sarasola, O. Dicuonzo, I. Ivashov, K. Sedlak, D. Uglietti, P. Bruzzone, Hybrid HTS-Nb_3Sn-NbTi DEMO CS coil design optimized for maximum magnetic flux generation, *Fusion Engineering and Design* **146** (2019) 10-13.

[11] CryoSoft THEA (Thermal, hydraulic and electric analysis of superconducting cables) User's Guide, version 2.4, January 2021, Horizon Technologies, Littleton - CO, United States of America. https://supermagnet.sourceforge.io/thea.html.

[12] P. Bruzzone, K. Sedlak, B. Stepanov, M. Kumar, V. D'Auria, A new cabled stabilizer for the Nb_3Sn react&wind DEMO conductor prototype, *IEEE Transactions on Applied Superconductivity* **31** (2021) 4802505.

[13] Shanghai Superconducting Technology Co. Ltd., Shanghai, China. http://www.shsctec.com.

[14] M. Mattei, DEMO AR = 3.1 preliminary breakdown magnetic analyses, 11th August 2015, https://idm.euro-fusion.org/?uid=2MXBK3.

[15] R. Guarino, R. Wesche, K. Sedlak, Assessment of the thermal-hydraulic performance of the European DEMO NbTi bus bars, *IEEE Transactions on Applied Superconductivity* **32** (2022) 4801705.

[16] M. Wilson, NbTi superconductors with low ac loss: a review, *Cryogenics* **48** (2008) 381-395.

[17] A. Dembkowska, M. Lewandowska, X. Sarasola, K. Sedlak, Quench analysis of the DEMO CS1 coil, *Cryogenics* **112** (2020) 103194.

[18] P. Bruzzone, R. Herzog, B. Stepanov, M. Vogel, R. Wesche, Test results of a large size, forced flow Nb_3Sn conductor, based on a design alternative to the cable-in-conduit, *IEEE Transactions on Applied Superconductivity* **17** (2007) 1473-1476.

[19] M.S. Bhatti, R.K. Shah, Turbulent and transition flow convective heat transfer in ducts, In: S. Kakac, R.K. Shah, W. Aung (Eds.), *Handbook of Single-Phase Convective Heat Transfer*, Wiley (1987).

[20] F.W. Dittus, L.M.K. Boelter, Heat transfer in automobile radiators of the tubular type, *University of California Publications in Engineering* **2** (1930) 443-461.

[21] C. Hoa, T. Latella, F. Bonne, B. Lacroix, Q. Le Coz, L. Zani, M. Lewandowska, K. Sedlak, V. Corato, Parametric study and optimization of the cryo-magnetic system for EU DEMO at the pre-conceptual design phase, *Cryogenics* **124** (2022) 103475.

[22] A. Dembkowska, M. Lewandowska, X. Sarasola, Thermal-hydraulic analysis of the DEMO CS coil, *IEEE Transactions on Applied Superconductivity* **28** (2018) 4205605.

[23] M. Lewandowska, K. Sedlak, Thermal-hydraulic analysis of LTS cables for the DEMO TF coil, *IEEE Transactions on Applied Superconductivity* **24** (2014) 4200305.

[24] M. Lewandowska, A. Dembkowska, R. Heller, M. Wolf, Thermal-hydraulic analysis of an HTS DEMO TF coil, *Cryogenics* **96** (2018) 125-132.

[25] A. Zappatore, R. Bonifetto, X. Sarasola, R. Zanino, Effect of local defects on HTS fusion magnets performance, *IEEE Transactions on Applied Superconductivity* **32** (2022) 4203809.

[26] D. Uglietti, N. Bykovskiy, K. Sedlak, B. Stepanov, R. Wesche, P. Bruzzone, Test of 60kA coated conductor cable prototypes for fusion magnets, *Superconductor Science and Technology* **28** (2015) 124005.

[27] L. Bottura, B. Bordini, $J_c(B,T,\varepsilon)$ parameterization for the ITER Nb_3Sn production, *IEEE Transactions on Applied Superconductivity* **19** (2009) 1521-1524.

[28] L. Bottura, A practical fit for the critical surface of NbTi, *IEEE Transactions on Applied Superconductivity* **10** (2000) 1054-1057.

Appendix A – Scaling law for the ReBCO tapes

The scaling law for the critical current density, written as function of the magnetic field B, the temperature T and the angle θ between magnetic field and tape, is given by:

$$J_c(B,T,\theta) = J_c(B,T)F(\theta) \quad \text{(A1)}$$

where [26]:

$$J_c(B,T) = \frac{A}{B}\left[\frac{B_{irr}(T)}{B_{irr}(0)}\right]^{\beta}\left[\frac{B}{B_{irr}(T)}\right]^{p}\left[1-\frac{B}{B_{irr}(T)}\right]^{q} \quad \text{(A2)}$$

whereas the dimensionless factor F is given by:

$$F(\theta) = 1 + 3.222\, e^{\frac{\theta-90}{8.234}} + 1.278\, e^{\frac{\theta-90}{0.5901}} \quad \text{(A3)}$$

In Equation (A1), B_{irr} is the irreversibility magnetic field, provided by the relation:

$$B_{irr}(T) = B_{irr}(0)\left(1-\frac{T}{T_c}\right)^{\alpha} \quad \text{(A4)}$$

where T_c is the critical temperature.

The numerical coefficients appearing in Equations (A1,A4) are reported in Table A1.

Table A1 Numerical coefficients employed in the scaling law for the ReBCO tapes.

Coefficient	Value
A	$3.7923 \cdot 10^{12}$ A T m^{-2}
α	1.5181
β	2.2351
p	0.50215
q	1.6983
$B_{irr}(0)$	120.0 T
T_c	92.833 K

Appendix B – Scaling law for the Nb_3Sn strands

In the case of the Nb_3Sn strands, the scaling law for the critical current density, written as function of the magnetic field B, the temperature T and the strain ε imposed to the superconducting filaments, is given by [27]:

$$J_c(B,T,\varepsilon) = \frac{C}{B}s(\varepsilon)(1-t^{1.52})(1-t^2)b^p(1-b)^q \quad \text{(B1)}$$

where the strain function is:

$$s(\varepsilon) = 1 + \frac{1}{1 - C_{a1}\varepsilon_{0,a}}\left[C_{a1}\left(\sqrt{\varepsilon_{sh}^2 + \varepsilon_{0,a}^2} - \sqrt{(\varepsilon - \varepsilon_{sh})^2 + \varepsilon_{0,a}^2}\right) - C_{a2}\varepsilon\right] \tag{B2}$$

with:

$$\varepsilon_{sh} = \frac{C_{a2}\varepsilon_{0,a}}{\sqrt{C_{a1}^2 - C_{a2}^2}} \tag{B3}$$

The functions *b* and *t* appearing in Equation (B1) are the reduced magnetic field and reduced temperature, respectively, and they are given by:

$$b = \frac{B}{B_{c2}^*(T,\varepsilon)} = \frac{B}{B_{c20max}^* s(\varepsilon)(1 - t^{1.52})} \tag{B4}$$

$$t = \frac{T}{T_C^*(0,\varepsilon)} = \frac{T}{T_{c0max}^*[s(\varepsilon)]^{\frac{1}{3}}(1 - t^{1.52})\left[1 - \left(\frac{B}{B_{c20max}^* s(\varepsilon)}\right)\right]^{\frac{1}{1.52}}} \tag{B5}$$

The numerical coefficients appearing in Equations (B1-B5) are reported in Table B1.

Table B1 Numerical coefficients employed in the scaling law for the Nb_3Sn strands.

Coefficient	Value
C_{a1}	45.74
C_{a2}	4.431
$\varepsilon_{0,a}$	0.232 %
B_{c20max}	29.39 T
T_{c0max}	16.48 K
C	$7.956 \cdot 10^{10}$ A T m^{-2}
p	0.556
q	1.698

Appendix C – Scaling law for the NbTi strands

In the case of the NbTi strands, the scaling law for the critical current density, written as function of the magnetic field *B* and the temperature *T*, is given by [28]:

$$J_c(B,T) = \frac{C_0}{B}\left[1 - \left(\frac{T}{T_{c0}}\right)^{1.7}\right]^{\gamma}\left[\frac{B}{B_{c2}(T)}\right]^{\alpha}\left[1 - \frac{B}{B_{c2}(T)}\right]^{\beta} \quad \text{(C1)}$$

where:

$$B_{c2}(T) = B_{c20}\left[1 - \left(\frac{T}{T_{c0}}\right)^{1.7}\right] \quad \text{(C2)}$$

The numerical coefficients appearing in Equations (C1,C2) are reported in Table C1.

Table C1 Numerical coefficients employed in the scaling law for the NbTi strands.

Coefficient	**Value**
C_0	$1.68512 \cdot 10^{11}$ A T m^{-2}
B_{c20}	14.61 T
T_{c0}	9.03 K
α	1.00
β	1.54
γ	2.10